THE JOURNAL OF
PHYSICAL CHEMISTRY
LETTERS
A JOURNAL OF THE AMERICAN CHEMICAL SOCIETY

Dissociation Time, Quantum Yield, and Dynamic Reaction Pathways in the Thermolysis of *trans*-3,4-Dimethyl-1,2-dioxetane

Jian-Ge Zhou,* Yinan Shu, Yuchen Wang, Jerzy Leszczynski,* and Oleg Prezhdo*

Cite This: *J. Phys. Chem. Lett.* 2024, 15, 1846−1855 Read Online

ABSTRACT: The thermolysis of *trans*-3,4-dimethyl-1,2-dioxetane is studied by trajectory surface hopping. The significant difference between long and short dissociation times is rationalized by frustrated dissociations and the time spent in triplet states. If the C−C bond breaks through an excited state channel, then the trajectory passes over a ridge of the potential energy surface of that state. The calculated triplet quantum yields match the experimental results. The dissociation half-times and quantum yields follow the same ascending order as per the product states, justifying the conjecture that the longer dissociation time leads to a higher quantum yield, proposed in the context of the methylation effect. The populations of the molecular Coulomb Hamiltonian and diagonal states reach equilibrium, but the triplet populations with different S_z components fluctuate indefinitely. Certain initial velocities, leading the trajectories to given product states, can be identified as the most characteristic features for sorting trajectories according to their product states.

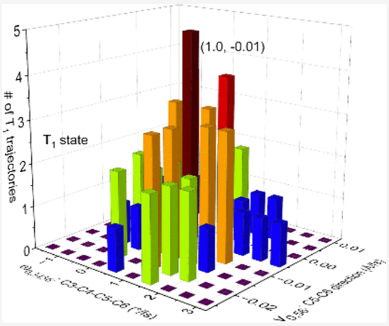

Chemiluminescence represents the emanation of light in a chemical reaction in which a molecule is thermally activated and experiences a nonadiabatic transition to an electronic excited state of the fragmentation product.[1−3] The process is called bioluminescence when it occurs in living organisms, e.g., fireflies. Chemiluminescence or bioluminescence has wide-ranging applications, such as treating cancers via photodynamic therapy,[4−6] acting as a bioluminescence imaging tool,[7,8] and tracking environmental pollutants.[9] The thermolysis of the four-membered heterocyclic peroxides, e.g., 1,2-dioxetane, generates electronically excited state carbonyl compounds that emit light to release the excess energy[1] (see Figure 1). The enhancement of the quantum yields of singlet and triplet chemiexcitation was achieved experimentally by the methylation of the 1,2-dioxetanes.[1,10] The chemiluminescent mechanism has been studied by computing potential energy surface (PESs), locating minima, transition states (TSs), and conical interactions and/or intersystem crossings, and identifying the potential reaction pathways.[11−18] The dynamical quantities, e.g., dissociation time and branching ratios, however, cannot be analyzed in the context of critical points and PESs. The high demand for the nonadiabatic molecular dynamics (NAMD) methods, in which the nuclear motion is regulated by multiple electronic states, has led to the development of different approaches.[19−33] As the full quantum-mechanical methods are expensive and limited to a few degrees of freedom,[33−35] the trajectory surface hopping (TSH)[19] method has emerged as one of the most popular tools for the NAMD simulations, which was used recently to study the chemiluminescent processes for the four-membered heterocyclic peroxides.[1]

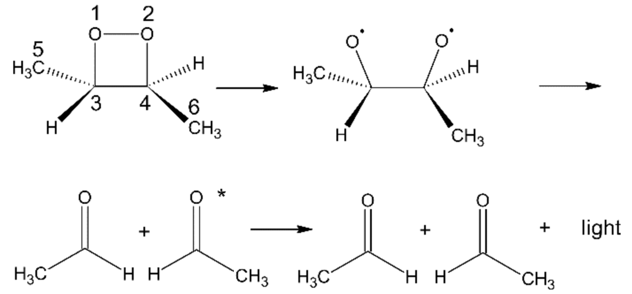

Figure 1. Thermolysis of *trans*-3,4-dimethyl-1,2-dioxetane into two acetaldehydes. The asterisk means that the molecule is in the excited state.

The thermal decomposition of 1,2-dioxetane derivatives was discussed via the TSH approach[36,37] implemented in the Newton-X package[38] interfaced with Molcas[39] (Newton-X/Molcas). The electronic structure method employed in Molcas[39] was the state-averaged complete active space self-consistent field (SA-CASSCF)[40] with the ANO-RCC-VTZP basis set[41] and state averaging over the four lowest singlet states in the active space of 12 electrons and 10 orbitals, i.e.,

Received: December 21, 2023
Revised: January 26, 2024
Accepted: February 6, 2024
Published: February 9, 2024

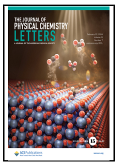

https://doi.org/10.1021/acs.jpclett.3c03578

SA4-CASSCF(12e,10o)/ANO-RCC-VTZP. It inferred that the 1,2-dioxetane molecule is trapped in the singlet excited states, and the decomposition process is deferred.[36] The methyl substitution of the 1,2-dioxetane increased the dissociation time via the mass effect in which the dissociation time was reproduced by the substitution groups with the same moment of inertia of the methyl group.[37] With the Newton-X/Molcas combined package, the quantum yield of *trans*-3,4-dimethyl-1,2-dioxetane (TDMD)[10] was estimated by the SA8-CASSCF(8e,6o)/STO-3G+6-31G* mixed basis set, including the four lowest singlet states and four lowest triplet states.[42] The obtained data revealed that the calculated quantum yield of the first triplet excited state (T_1) was comparable to the experimental result,[10] and the quantum yield of the second singlet excited state (S_2) was greater than that of the first singlet excited state (S_1). Including the triplet excited states in the TSH simulation increases the dissociation half-time enormously, and this is the reason that the small active space and mixed basis set were selected.[42] Even with these achievements, some questions are still unclear. (1) As the fragmentation product of the trajectories, i.e., the acetaldehyde molecule (Figure 1), can be in different energy states (e.g., T_1, S_0, or S_1), what is the order of the dissociation times as per the product energy states, or what state has the longest dissociation half-time? (2) Why do some trajectories have short dissociation times, some long, and is it related to the initial conditions of trajectories? (3) Why is the quantum yield of the S_2 product state greater than that of the S_1 product state, and what mechanism is behind this anomaly? (4) After the molecule escapes the entropic trap region[12,36] in which the four lowest singlet states and four lowest triplet states are nearly degenerated, do the surface hops still take place, and can the populations of the triplet states with different z components of the spin reach the constant values after a certain time period? (5) Are there some traits that make it most obvious for them to assort the trajectories according to their product energy states?

Guided by these questions, in this work we study the dynamic thermolysis of the TDMD molecule by the TSH method[19] implemented in the SHARC package[43−45] interfaced with OpenMolcas.[46] One of the strengths of the SHARC is that it processes internal conversion and intersystem crossing on the same footing by combining the spin−orbit-free input energies, gradients, and nonadiabatic couplings with the spin−orbit matrix elements in a spin−orbit-free electronic basis. As the decomposition of the TDMD can be characterized by the O1−O2−C3−C4 dihedral angle (Figure 1), we evaluate the distribution of the trajectories over this dissociation dihedral angle and dissociation time, minimum and maximum dissociation times, and dissociation half-time to demonstrate the allocation of the trajectories, and the order of the dissociation times as per their product energy states. The time evolutions of the C3−C4 distance, the O1−O2−C3−C4 dihedral angle, the potential energy of the active state, the number of frustrated dissociations, and the time spans in the singlet and triplet states along the short and long trajectories are calculated to explain the significant dissociation time difference between the short and long trajectories and address the cause of delay of the decomposition process. We compute the time evolutions of the ensemble-averaged populations of the MCH (molecular Coulomb Hamiltonian) and diagonal states[44] to examine the quantum yields for the respective product energy states and check the population equilibrium of the triplet excited states with different z components of the spin. To explore how the product energy state of the trajectories stochastically correlates with the initial velocities, we evaluate the distribution of the number of the trajectories over the initial velocities and dissociation time to determine if in the initial velocities there are the most characteristic features that are easiest to use to separate the trajectories as per their product energy states.[47]

For the evaluation of electronic structure of the biradicals in the thermolysis of the TDMD, the SA-CASSCF approach[40] with state averaging over states S_0−S_3 and T_1−T_4 was applied to optimize the transition states, evaluate the normal modes at the transition states, and compute the potential energy and its first derivative with respect to nuclear coordinates along the trajectories. The selected active space consists of the 12 electrons distributed in 10 orbitals, i.e., the four σ and four σ^* orbitals of the four-membered ring and the two oxygen lone-pair orbitals perpendicular to the ring.[36,37] The 6-31G basis set[48] was employed in the optimization and NAMD simulation, i.e., SA8-CASSCF(12e,10o)/6-31G. The dynamic process starting from the O−O transition state (Figure 1 and Figure S1) can be simulated by the SA-CASSCF method (see Figure S2).

We conducted the NAMD simulations by the fewest-switches trajectory surface hopping[19] with energy-based decoherence correction[49−51] implemented in SHARC 2.1.[43−45] The nuclear equations of motion were integrated by the velocity-Verlet algorithm[52] with a time step size of 0.5 fs and propagated by using the projected nonadiabatic couplings as the direction to adjust the momentum after the trajectory hops.[53] The electronic structure is handled quantum mechanically by solving the time-independent Schrödinger equation, and the nuclei propagate in trajectories governed by multiple potential energy surfaces. The total Hamiltonian for intersystem crossing dynamics in the SHARC is written as $H^{\text{total}} = H^{\text{MCH}} + H^{\text{SOC}}$, where H^{MCH} is the nonrelativistic molecular Coulomb Hamiltonian (MCH) and the H^{SOC} is the spin−orbit coupling operator.[54] The eigenstates of H^{MCH} are denoted as the MCH states, e.g., states S_0 and $T_{1,-1}$, in which the total electron spin S and its z component S_z are good quantum numbers. If the spin−orbit couplings (SOCs) are included,[54] there are two drawbacks in the MCH representation. (1) The off-diagonal couplings in H^{total} are usually delocalized over the PES, which results in the non-zero transition probability even far from crossing regions; thus, a much larger number of trajectories are needed to sample the process correctly because surface hops may occur in a much larger phase space volume.[44] (2) The sum of the transition probabilities over all multiple components depends on the rotation of the molecule in the laboratory frame.[55] To overcome these shortcomings, the diagonal basis is selected, which is the set of eigenstates of H^{total}, i.e., diagonal states.[44] All couplings between the diagonal states are described by a nonadiabatic coupling vector. To simulate the nonadiabatic dynamics of the thermal decomposition of the TDMD effectively, all sampling trajectories start from the rate-controlling O−O bond-breaking transition state (TS_{O-O}) in the S_0 state (Figure 1 and Figure S1) and have the same initial coordinates of TS_{O-O}, but the initial velocities are generated by the random sampling algorithm proposed by Sellner, Barbatti, and Lischka (SBL).[56] The initial kinetic energy at TS_{O-O} (3.96 eV) is the zero-point vibrational energy of TS_{O-O} (3.35 eV, computed via SA-CASSCF) plus the CASPT2 correction

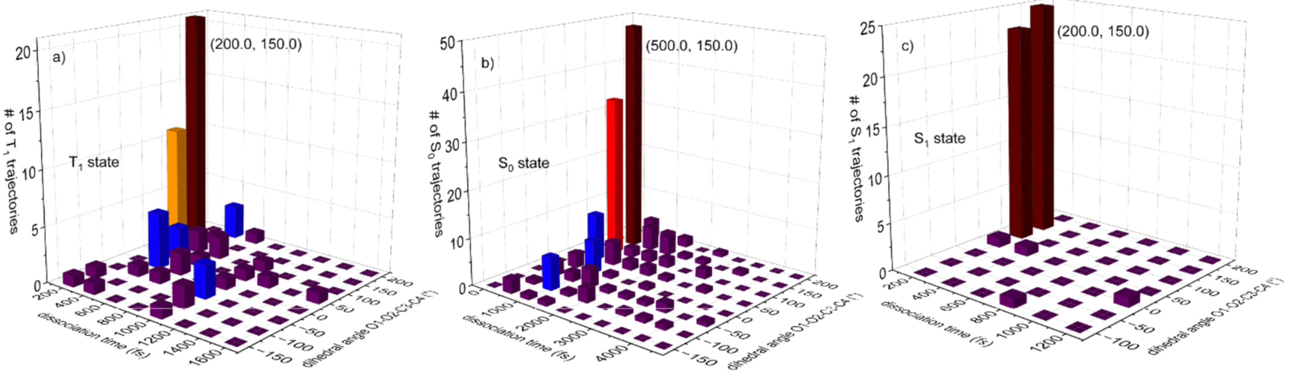

Figure 2. Distribution of the number of trajectories over the dissociation time (femtoseconds) and O1−O2−C3−C4 dissociation dihedral angle (degrees) for the (a) T_1, (b) S_0, and (c) S_1 product states.

energy (see the Supporting Information). First, the initial velocities are sampled by the Boltzmann distribution at 300 K, and then the initial kinetic energies of all of the trajectories at TS_{O-O} are rescaled to the same energy (3.96 eV). In the O−O reaction coordinate with the imaginary frequency, the sampled velocities, forward to the product direction, are selected for the NAMD simulation. We have coded the SBL sampling algorithm in SHARC. The C−C van der Waals bond length is 2.4 Å, and the trajectories are forced to be terminated if the distance between the C3 and C4 atoms is >3.7 Å. The electronic energies, nuclear gradients, and SOCs are all computed using OpenMolcas 21.06[46] that is interfaced with SHARC version 2.1.[43−45]

In the NAMD simulation, we consider the S_0−S_3 and T_1−T_4 states among which the surface hopping to state T_3 or T_4 is turned off to reduce the computational cost and simulation time. Of the 310 trajectories, 302 trajectories terminated successfully with a C3−C4 distance of >3.7 Å, and eight trajectories failed because of the lack of conservation of energy. All trajectories end in the T_1, S_0, and S_1 product state, and no trajectory was found in the other states. The MCH state of the trajectory labeled at the time of the cleavage of the C3−C4 bond (it just becomes greater than 2.4 Å) remains unchanged after the C3−C4 bond breaks. For example, if the MCH state of the trajectory is T_1 around 2.4 Å of the C3−C4 distance, the trajectory follows the T_1 state until it reaches 3.7 Å (the S_z components still change). The distribution of the number of the completed trajectories over the dissociation time (the time needed when the C−C distance evolves to 2.4 Å) and O1−O2−C3−C4 dissociation dihedral angle in Figure 2 shows that (1) the maximum dissociation times for the T_1, S_0, and S_1 trajectories, which have corresponding T_1, S_0, and S_1 product state, are ∼1600, ∼4500, and ∼1200 fs respectively; (2) the most prevalent dissociation dihedral angles are almost the same for the T_1, S_0, and S_1 trajectories and are around 150.0° (the initial dihedral angle is 135.8°; the most populated angle variation between the final and initial dihedral angle of the trajectories is 14.2°) and the most populated trajectories have short dissociation times; (3) the O1−O2−C3−C4 dissociation dihedral angle of the trajectories is distributed from −180° to 0° to 180° (−180° is equal to 180° in a dihedral angle); and (4) most S_1 trajectories have short dissociation times.

The minimum and maximum dissociation times, dissociation half-times, means, and standard deviations are listed in Table 1 for the T_1, S_0, and S_1 product states. The dissociation half-time is the time required for half of the trajectories to dissociate. Table 1 indicates that the S_0 trajectories have the longest dissociation half-time of 253.25 fs, and the S_1 trajectories have the shortest dissociation half-time of 64.50 fs. Both orders of the dissociation half-times and maximum dissociation times are the same for the T_1, S_0, and S_1 product states. The maximum dissociation time perhaps provides the time scale for the chemiluminescent decomposition. For the S_0 trajectories, the shortest trajectory takes only 39.00 fs for dissociation to occur, but the longest one needs 4329.00 fs to break the C3−C4 bond. The dissociation time difference between the long and short S_0 trajectories is significant, and similar conclusions hold for the T_1 and S_1 trajectories.

Table 1. Minimum and Maximum Dissociation Times, Dissociation Half-Times, Means, and Standard Deviations (femtoseconds) for the T_1, S_0, and S_1 Product States

	T_1	S_0	S_1	all trajectories
minimum dissociation time	46.50	39.00	44.50	39.00
maximum dissociation time	1566.50	4329.00	1155.00	4329.00
dissociation half-time	196.00	253.25	64.50	178.00
mean	343.82	667.01	111.43	496.44
standard deviation	320.65	860.21	176.80	720.08

To see how the short and long trajectories behave differently in their dissociation times, we study the time evolutions of the C3−C4 distance and the O1−O2−C3−C4 dihedral angle (Figure 3a,b). For the T_1 short trajectory (trajectory 69, a representative of the T_1 short trajectories) whose product state is T_1, the C3−C4 distance increases almost monotonously with time; however, the dihedral angle changes from 135.8° to 128.9°, and the angle variation is 6.9°, which demonstrates that this T_1 short trajectory dissociates without any frustrated dissociation.[36] At 44.0 fs, the T_1 short trajectory is on the PES of the T_1 state, its potential energy reaches the maximum [3.27 eV (Figure 3c)], and the corresponding C3−C4 distance is 2.16 Å (Figure 3a), which is greater than 2.08 Å, which is the C3−C4 distance of the C−C transition state on the T_1 PES (Figure S1c). At 42.5 fs, the dihedral angle arrives at its local maximum. Before 42.5 fs, the dihedral angle increases, and at 42.5 fs, the dihedral angle begins to decrease to prepare the configuration to pass over the ridge of the T_1 PES between TS_{O-O} and the dissociated TDMD, which is termed the T_1 ridge (the crossing point over this T_1 ridge is the potential energy peak at 44.0 fs). Most peaks (e.g., at 18.5 fs) along the

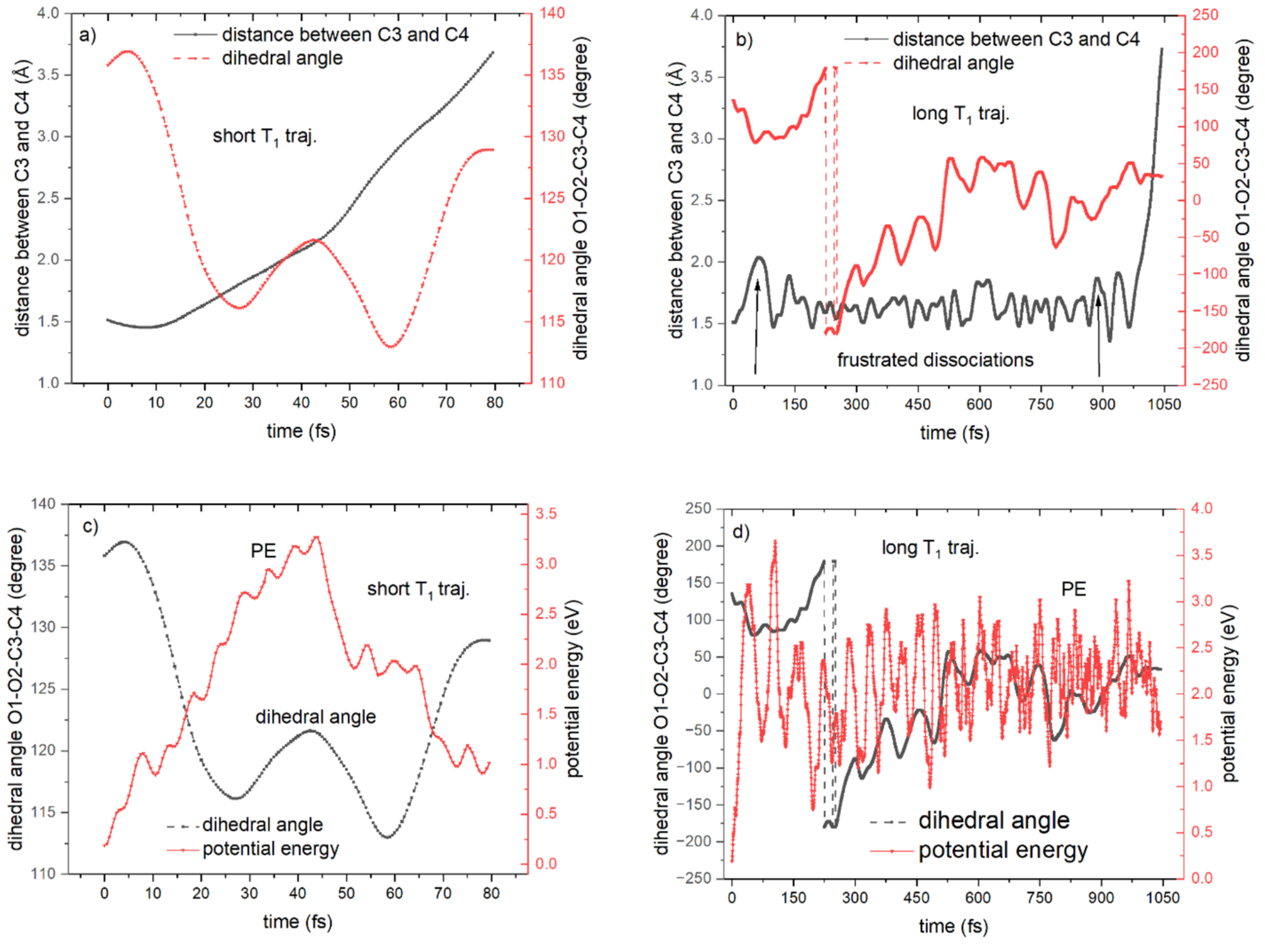

Figure 3. Time evolutions of the C3−C4 distance (angstroms) and O1−O2−C3−C4 dihedral angle (degrees) for (a) a T_1 short trajectory and (b) a T_1 long trajectory. The peaks along the C3−C4 curve represent the frustrated dissociations, and the vertical arrows indicate two frustrated dissociations. Time evolution of the O1−O2−C3−C4 dihedral angle and the potential energy (electronvolts) of the active state for (c) a T_1 short trajectory and (d) a T_1 long trajectory.

potential energy curve of the active state represent the surface hops between the diagonal states, in which the dihedral angles at the corresponding times of the potential energy peaks do not display the locally minimal or maximal values. The nonadiabatic transitions between the MCH states in this T_1 short trajectory are listed in Table 2. The diagonal element represents the number of transitions within a MCH state (step i to step $i + 1$ within a MCH state is counted as one transition), and the off-diagonal element shows the number of surface hops between two different MCH states. The total steps in a MCH state are the diagonal element of this state plus the number of the surface hops from all other states to this state, which is the sum of all of the off-diagonal elements along the column in which this state resides (Table 2) (see the Supporting Information for details).

Table 2. Numbers of Nonadiabatic Transitions among the MCH States in the T_1 Short Trajectory

	S_0	S_1	S_2	S_3	$T_{1,-1}$	$T_{2,-1}$	$T_{1,0}$	$T_{2,0}$	$T_{1,1}$	$T_{2,1}$
S_0	59	0	0	0	1	0	0	0	0	0
S_1	1	10	0	0	0	0	0	0	0	0
S_2	0	0	0	0	0	0	0	0	0	0
S_3	0	0	0	0	0	0	0	0	0	0
$T_{1,-1}$	1	0	0	0	5	0	0	1	0	0
$T_{2,-1}$	0	1	0	0	0	0	0	0	0	0
$T_{1,0}$	0	0	0	0	0	0	0	0	0	0
$T_{2,0}$	0	0	0	0	0	1	0	1	0	0
$T_{1,1}$	0	0	0	0	1	0	0	0	60	1
$T_{2,1}$	0	0	0	0	0	0	0	0	1	15

The C3−C4 bond in this T_1 short trajectory takes 159 steps, i.e., 79.5 fs (step size of 0.5 fs), to reach 3.7 Å. From Table 2, we find that the T_1 short trajectory spends 30.5 fs (61 steps), 5.5 fs, 34.0 fs, and 9.5 fs in states S_0, S_1, T_1, and T_2, respectively, and stays in the T_1 state with the longest time. This T_1 short trajectory (1) starts from TS_{O-O} on the S_0 PES; (2) passes through the entropic trap region by hopping among the S_0, S_1, T_1, and T_2; and (3) climbs on the T_1 PES and passes over the T_1 ridge. In other words, the molecule is dissociated with the T_1 product state. In general, in the early stage the trajectory is mainly in the S_0 state; later, it spends its most time in the T_1 state with the surface hops among the T_1 states with different z components of the spin [$S_z = -1$, 0, or 1; i.e., $T_{1,-1}$, $T_{1,0}$, and $T_{1,1}$ (the energy gaps among $T_{1,-1}$, $T_{1,0}$, and $T_{1,1}$ are small even out of the entropic trap region), and finally, it overcomes the T_1 ridge.

For the T_1 long trajectory (trajectory 23), the dihedral angle changes from 135.8° to 180° (−180°) to −90° to 0° to 32.9° and the angle variation is 257.1°. A dihedral angle takes a value in the ranges of 0° to 180° and 0° to −180° instead of 0° →

Table 3. Numbers of Nonadiabatic Transitions among the MCH States in the T_1 Long Trajectory

	S_0	S_1	S_2	S_3	$T_{1,-1}$	$T_{2,-1}$	$T_{1,0}$	$T_{2,0}$	$T_{1,1}$	$T_{2,1}$
S_0	51	0	1	0	2	0	5	1	0	0
S_1	4	203	4	1	2	1	0	8	1	3
S_2	0	4	42	0	1	0	0	1	0	1
S_3	0	0	1	24	0	0	0	0	0	0
$T_{1,-1}$	3	1	0	0	474	3	14	1	16	2
$T_{2,-1}$	0	4	0	0	3	176	0	8	1	10
$T_{1,0}$	2	3	0	0	14	0	266	4	16	0
$T_{2,0}$	0	8	0	0	1	7	4	219	0	9
$T_{1,1}$	1	0	0	0	16	1	15	1	239	1
$T_{2,1}$	0	4	1	0	1	14	0	5	1	158

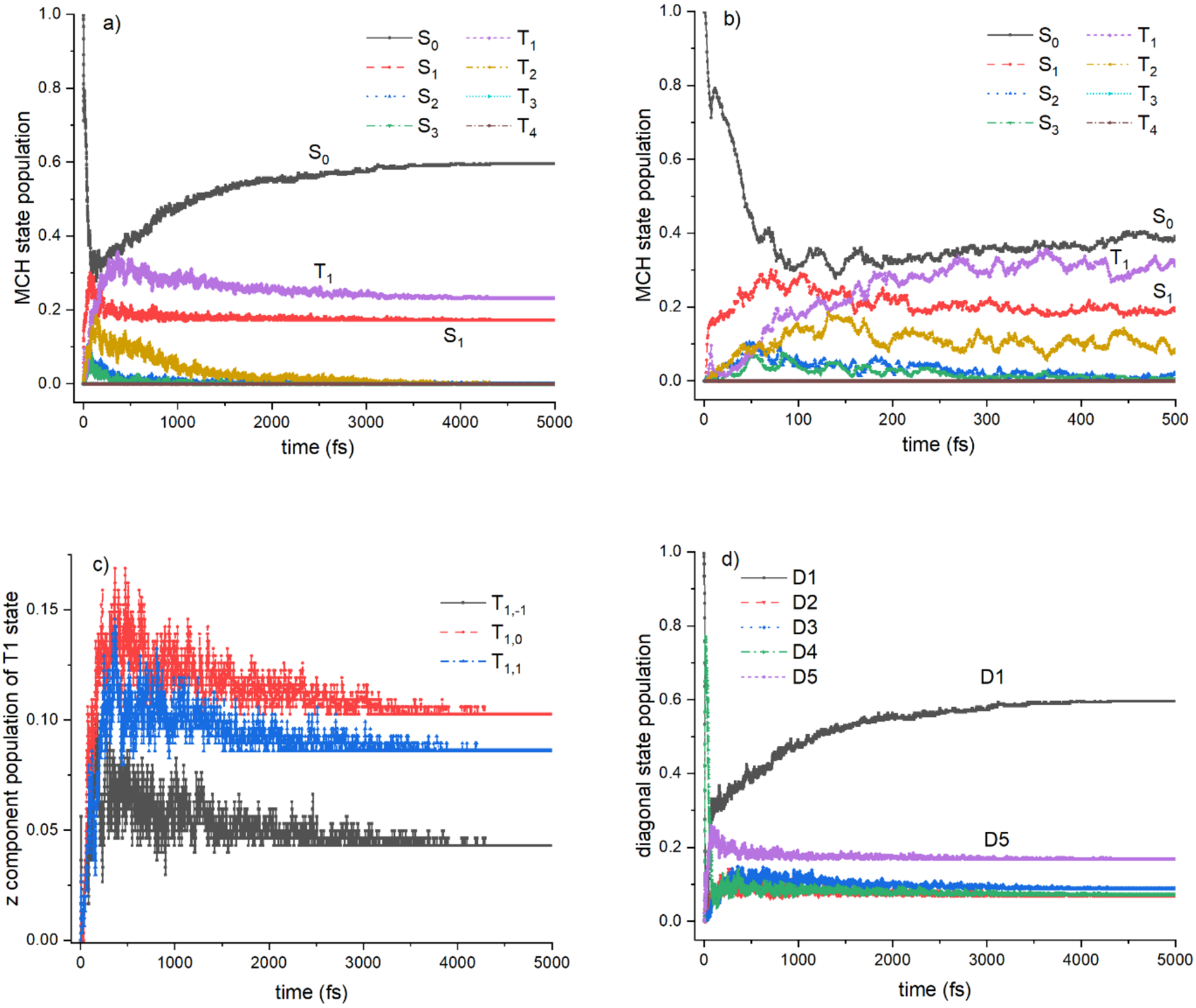

Figure 4. Time evolutions of (a) the populations of the MCH states in 5000 fs, (b) the populations of the MCH states in 500 fs, (c) the populations of states $T_{1,-1}$, $T_{1,0}$, and $T_{1,1}$, and (d) the populations of the diagonal states.

180° → 360°; in other words, 180° equals −180°. If an angle oscillates between 178° and 183°, however, for the dihedral angle, it acts as if it is oscillating between 178° and −177°, so it looks discontinuous but continuous geometrically, which explains why the time evolution of the dihedral angle in Figure 3b appears discontinuous between 180° and −180°. The C3−C4 distance oscillates around 1.6 Å, and there are 24 frustrated dissociations within 975.5 fs, which are identified by the local maxima in the time evolution of the C3−C4 bond length [the number of the peaks along the curve of the C3−C4 distance is that of the frustrated dissociations (see Figure 3b)].[36] The average oscillation period is 40.6 fs (975.5/24) which matches the C−C vibration in the biradical region. In Figure 3d, there are ∼24 noticeable potential energy peaks, which means that each frustrated dissociation can be visualized as the oscillation between the two adjacent local maxima of the potential energy curve. The global maximal potential energy along the T_1 long trajectory is 3.66 eV located at 105.5 fs; however, it is on the T_2 PES, and the molecule does not dissociate by overcoming the T_2 ridge. The T_1 long trajectory hops among states S_0−S_3, T_1, and T_2 in the entropic trap region and stochastically seeks its dynamic reaction path. At 966.5 fs, the trajectory is on the T_1 PES, and the potential energy reaches the second highest peak [3.22 eV (Figure 3d)], which is identified as the other crossing point over the T_1 ridge. At the same time, the dihedral angle attains its peak (∼966.5 fs), which means that the C3−C4 bond starts to break upon adjustment of the dihedral angle from increasing to decreasing (Figure 3b). After 966.5 fs, the C3−C4 distance rapidly increases to 3.7 Å. From Table 3, we find that the T_1 long trajectory spends 30.5, 113.5, 24.5, 12.5, 546.0, and 317.0 fs in states S_0−S_3, T_1, and T_2, respectively. For the most time, the T_1 long trajectory stays in the T_1 and T_2 states and hops among states $T_{1,-1}$, $T_{1,0}$, $T_{1,1}$, $T_{2,-1}$, $T_{2,0}$, and $T_{2,1}$; however, the molecule does not dissociate through the T_2 ridge, and the C−C bond breaks by passing over the T_1 ridge.

For the S_0 short trajectory (trajectory 138), at 28.5 fs the potential energy arrives at its global maximum peak [2.86 eV (Figure S4a)], but it is on the S_3 PES. One femtosecond later (at 29.5 fs), the trajectory jumps to the S_0 PES and the C3−C4 bond starts to break (there is no local maximum on the S_0 PES when the C3−C4 distance is between 2.1 and 2.4 Å); i.e., the dissociation does not encounter the S_0 ridge. From Table S1, we discern that the S_0 short trajectory spends 60.1%, 21.0%, 1.5%, 15.9%, and 1.5% of the simulation time in states S_0−S_3 and T_2, respectively; in other words, it stays mainly in state S_0. From Table S2, we find that the S_0 long trajectory (trajectory 4) spends its most time in states T_1 and T_2 (46.0% and 32.3%, respectively) and 10.1%, 7.2%, 2.7%, and 1.7% in states S_0−S_3, respectively. Just before 4298.5 fs, the trajectory was wandering in the T_2 state and then jumps to $S_3 \rightarrow S_2 \rightarrow S_1 \rightarrow S_0$ in the short time period, and the molecule dissociates on the S_0 PES without overcoming any local S_0 maximum along the potential energy curve (Figures S3b and S4b). The molecule that breaks the C−C bond through the S_0 PES does not encounter the S_0 ridge, which is consistent with the reaction coordinate analysis that after TS_{O-O}, the C−C bond breaking transition states on the S_1−S_3 and T_1−T_4 PES exist, but there is no TS_{C-C} on the S_0 PES.[12,36] Between 0.0 and 4300.0 fs, there are 108 frustrated dissociations in the C3−C4 bond oscillation (Figure S4b), and the period is 39.8 fs, which is consistent with the C−C vibration. The 108 frustrated dissociations make this trajectory take a long time to dissociate.

At 38.0 fs, the C3−C4 distance is 2.16 Å, and the S_1 short trajectory (trajectory 88) is in the S_1 state and reaches its global maximum (3.19 eV) of the potential energy (Figures S3c and S4c). Thus, the molecule dissociates by crossing the S_1 ridge located at 38.0 fs. From Table S3, we find that the S_1 short trajectory spends 37.9% of the time in state S_0, 2.1% in state T_1, and the highest percentage, 60.0%, in state S_1 and dissociates along the S_1 PES. The S_1 long trajectory (trajectory 253) spends 16.4%, 15.2%, 3.4%, 6.0%, 37.4%, and 21.6% in states S_0−S_3, T_1, and T_2, respectively (Table S4); in other words, for the most time, it stays in the triplet excited states. At 1147.0 fs, the S_1 long trajectory is on the S_1 PES and reaches its local maximum of the potential energy (2.85 eV) and the corresponding the C3−C4 distance is 2.16 Å (Figures S3d and S4d); thus, we infer this is the other crossing point over the S_1 ridge. After 1147.0 fs, the C3−C4 bond rapidly breaks. Within 1147.0 fs, the C3−C4 bond oscillates 24 times, and the oscillation period is 47.8 fs, which is comparable with that of the C−C bond vibration.

The average total number of hops among all states is 98.9 per trajectory, but the average total number of nonadiabatic transitions among states $T_{1,-1}$, $T_{1,0}$, $T_{1,1}$, $T_{2,-1}$, $T_{2,0}$, and $T_{2,1}$ states is 61.2 per trajectory, which indicates that most hops in trajectories are among the triplet states because of the small energy gaps among states $T_{1,-1}$, $T_{1,0}$, and $T_{1,1}$ (or $T_{2,-1}$ $T_{2,0}$, and $T_{2,1}$). The short trajectories spend a small amount of time in the triplet states, and the C−C bond breaks directly; however, the long trajectories stay in the triplet states for the most time with multiple frustrated dissociations.

The ensemble-average time evolutions of the MCH state populations for states S_0−S_3, T_1, and T_2 are illustrated in Figure 4a, which shows the population equilibrium after 4200 fs. The equilibrium populations for states T_1, S_0, and S_1 are 23.2%, 59.6%, and 17.2%, respectively, and are zero for other states. The previous research[42] found that the quantum yield of state S_2 was greater than that of state S_1. This anomalous phenomenon is not observed here. One possible reason is the use of the small active space and low-level basis set in the previous work,[42] which underestimates the transition probability from state S_2 to lower states. Panels a and b of Figure 4 show that the state S_0 population (1) decreases from 100% to 29.8% within 95.5 fs, (2) fluctuates between 95.5 and 190.5 fs, and (3) increases between 190.5 and 4200.0 fs and reaches a constant value 59.6% after 4200.0 fs. The S_1 population increases and arrives at its maximum of 30.1% at 71.0 fs, then decreases to 17.2% at 3979.5 fs, and finally reaches its equilibrium. The state S_2 and S_3 populations increase and achieve their maximum values of 10.3% at 48.0 fs and 7.6% at 49.5 fs, respectively, and then go to zero after 2186.5 fs. The T_2 population increases and reaches its maximum of 18.5% at 132.0 fs and then decreases and vanishes after 3668.0 fs. The T_1 population increases and reaches its maximum of 34.8% at 365.5 fs, decreases, and reaches its equilibrium 23.2% after 4200.0 fs. States S_0−S_3 and T_1−T_4 are not degenerated around the TS_{O-O} structure, and the S_0 state jumps more easily to state S_1 than to state T_1, which explains that before 95.5 fs, the S_1 population grows faster than the T_1 population. Later, the trajectories enter the entropic trap region, hopping to state T_1 becomes easier than before, and the trajectories accumulate favorably on the T_1 PES (see Table 3), which elucidates that the T_1 population exceeds the S_1 population after 157.0 fs.

The fragmentation product of the trajectories retains its MCH state (ignoring the difference among triplet states with different S_z values; in other words, $T_{1,-1}$, $T_{1,0}$, and $T_{1,1}$ are termed T_1) as that labeled at the C−C bond cleavage. If the product is in state S_0 or S_1, after scission of the C−C bond, there is no surface hopping in the trajectory. However, if the product is in state T_1, the surface hops among states $T_{1,-1}$, $T_{1,0}$, and $T_{1,1}$ continue after the C−C bond breaks. Two types of the surface hops occur: (1) between different diagonal states belonging to different MCH states, e.g., second diagonal state ($T_{1,0}$) → third diagonal state ($T_{1,1}$) (the second diagonal state is approximated as the $T_{1,0}$ state in the MCH representation, and the third diagonal state corresponds to the $T_{1,1}$ state), and (2) between different diagonal states belonging to the same MCH state, e.g., fourth diagonal state ($T_{1,0}$) → third diagonal state ($T_{1,0}$). Figure 4c indicates that the populations of states $T_{1,-1}$, $T_{1,0}$, and $T_{1,1}$ fluctuate around 4.3%, 10.3%, and 8.6%, respectively; in other words, they cannot reach population equilibrium because of the small energy differences among them. $T_{1,0}$ is the most populated and the $T_{1,-1}$ the least populated among states $T_{1,-1}$, $T_{1,0}$, and $T_{1,1}$.

Comparing panels a and c of Figure 4 with panel d, we find that the first diagonal state, D1, which is the lowest state in the diagonal representation, mainly contributes to state S_0 and the major component of state D5 comes from state S_1. Furthermore, the major parts of states D2−D4 correspond to states $T_{1,-1}$, $T_{1,0}$, and $T_{1,1}$, respectively, but the populations of states D2−D4 can reach equilibrium after 3500 fs. At the TS_{O-O} configuration, state S_0 has the lowest energy among states S_0−S_3 and T_1−T_4. Between 6.0 and 15.0 fs, most trajectories (77% of the total number of the trajectories) jump from the first diagonal state (S_0) to the fourth diagonal state (S_0) via internal conversion, which implies that state S_0 evolves from the lowest state (D1) to the fourth lowest state (D4) and the three z components of state T_1 possess energies that are lower than that of state S_0 in this part of the entropic trap region. This explains why there is a population peak (77.2%) of state D4 (S_0) around 11.0 fs (see Figure 4d). Here we point out that for most of the time, state D4 corresponds to state $T_{1,1}$ and state D1 matches state S_0.

The number of trajectories, the quantum yields, and the dissociation half-times for the product MCH states are listed in Table 4. The quantum yields for states S_2, S_3, and T_2 are zero, and the calculated quantum yield of state T_1 is 23.2%, which matches the experimental value (20.0%). The simulated quantum yield of the singlet excited states (S_1+S_2) is 17.2%, which is comparable with the value of 10.1% obtained by the SA8-CASSCF(8e,6o)/STO-3G+6-31G* method.[42] Table 4 shows that for states S_0, S_1, and T_1, the order of the quantum yields is the same as that of the dissociation half-times, which supports the argument that the longer dissociation time should cause the higher quantum yield observed in the mass effect of the methylation.[37]

Table 4. Numbers of Trajectories, Quantum Yields, and Dissociation Half-Times (femtoseconds) for the Product Energy States

	S_0	S_1	S_2	S_3	T_1	T_2
number of trajectories	180	52	0	0	70	0
quantum yield (%)	59.6	17.2	0	0	23.2	0
dissociation half-time	253.25	64.50	−	−	196.00	−

To examine whether the product energy states of the dissociated TDMD are related to the initial velocities, first we evaluate the distributions of the S_0, S_1, and T_1 trajectories over the dissociation time and the initial angular velocity of the O1−O2−C3−C4 (or C3−C4−C5−C6) dihedral angle, denoted as $\omega_{0,1234}$ (or $\omega_{0,3456}$) in Figure 5. The $\omega_{0,1234}$ coordinates of the most populated T_1, S_0, and S_1 trajectories are ∼0°/fs (Figure 5a−c); in other words, the highest peaks of product states T_1, S_0, and S_1 cannot be distinguished by $\omega_{0,1234}$. The range of $\omega_{0,1234}$ for all trajectories is $-3.0 \leq \omega_{0,1234} \leq 2.0$; i.e., its range length is 5.0. The subranges are $-3.0 \leq \omega_{0,1234} \leq 1.5$, $-2.0 \leq \omega_{0,1234} \leq 2.0$, and $-2.5 \leq \omega_{0,1234} \leq 1.0$ for the T_1, S_0, and S_1 trajectories, respectively. In the subrange adjacent to the negative end point, $-3.0 \leq \omega_{0,1234} < -2.0$, whose length (1.0) is 20.0% of the range length (5.0) [this ratio characterizes the relative length of the subrange near an end point (RLSE)], there is no S_0 trajectory; thus, the trajectories with the $\omega_{0,1234}$ close to the negative end point tend to evolve into product states S_1 and T_1. In the subrange $1.0 \leq \omega_{0,1234} < 2.0$ with a 20.0% RLSE, there is no S_1 state; thus, the trajectories with the $\omega_{0,1234}$ neighboring the positive end develop most likely to states T_1 and S_0. From the $\omega_{0,1234}$ side view, the number of trajectories on the left side of the highest peak is greater than that on the right side of the highest peak for states T_1, S_0, and S_1, which is attributed to the normal mode along the O1−O2 reaction coordinate being assigned with positive initial velocities to ensure molecular dissociation.

The $\omega_{0,3456}$ coordinates of the highest peaks of the T_1, S_0, and S_1 trajectories are 0.5°/fs, 1.5°/fs, and 1.0°/fs, respectively; in other words, the most populated T_1, S_0, and S_1 trajectories can be distinguished by the $\omega_{0,3456}$ coordinate (Figure 5d−f). In the subrange $-2.0 \leq \omega_{0,3456} < -1.0$ with a 20.0% RLSE, there is no T_1 trajectory; thus, the trajectories with the $\omega_{0,3456}$ vicinal to the negative end tend to product states S_0 and S_1. Furthermore, Figure S5 shows that (1) the trajectories with the $\nu_{0,12}$ (initial velocity of O1−O2) near the lower end (25.0% RLSE) incline to state S_0, (2) the trajectories with the $\nu_{0,12}$ adjacent to the upper end (12.5% RLSE) evolve least likely to state T_1, (3) the trajectories with the $\nu_{0,34}$ (initial velocity of C3−C4) vicinal to the negative end (23.1% RLSE) are apt to the singlet states, (4) the trajectories with the $\nu_{0,34}$ close to the positive end (23.1% RLSE) tend to states T_1 and S_0, and (5) the trajectories with the $\nu_{0,56}$ (initial velocity of C5−C6) neighboring to the positive end (33.3% RLSE) lean toward states S_0 and S_1. The initial dihedral angular velocities and/or initial velocities that take values near certain end points with considerable RLSE, e.g., the $\nu_{0,56}$ adjacent to the positive end (33.3% RLSE), can be identified as the most characteristic features in trajectories, which incline to the given energy state, and their final energy states are "easiest" to classify.[47]

In conclusion, the thermal decomposition of *trans*-3,4-dimethyl-1,2-dioxetane has been studied by the TSH dynamic approach. The significant difference in the dissociation time between the long and short trajectory has been elucidated by the time spent in the triplet states and the number of frustrated dissociations, which can be regarded as the C−C bond oscillation between two adjacent local maxima of the potential energy of the active state. Adding the singlet excited states to the NAMD simulation postpones the dissociation by introducing several frustrated dissociations. However, inclusion of the triplet states with different S_z components results in more than a hundred frustrated dissociations, which delays the chemiluminescent decomposition remarkably. When the molecule ruptures its C−C bond through the excited state channel, e.g., T_1 or S_1, it has to pass over the T_1 or S_1 ridge to reach the corresponding energy product. The ground state ridge has not been found. The simulated quantum yield of state T_1 matches the experimental result well. The dissociation half-times have been classified by the product energy states, and the order of the dissociation half-times is the same as that of the quantum yields for states T_1, S_0, and S_1. This result provides evidence for the conjecture that the longer decomposition time leads to the higher quantum yield observed in the context of the mass effect of methylation. After the dissociation, the degeneracy of the ground and excited states has been lifted, and the label of the product energy state in terms of states T_1, S_0, and S_1 has remained unchanged; thus, the ensemble-averaged populations of the MCH and diagonal states can reach equilibrium. Due to small energy gaps among states $T_{1,-1}$, $T_{1,0}$, and $T_{1,1}$ (or $T_{2,-1}$, $T_{2,0}$, and $T_{2,1}$), surface hops still exist even after the dissociation, and the populations of the triplets with different S_z components oscillate around certain values. The distribution of the trajectories over the initial velocities has revealed that

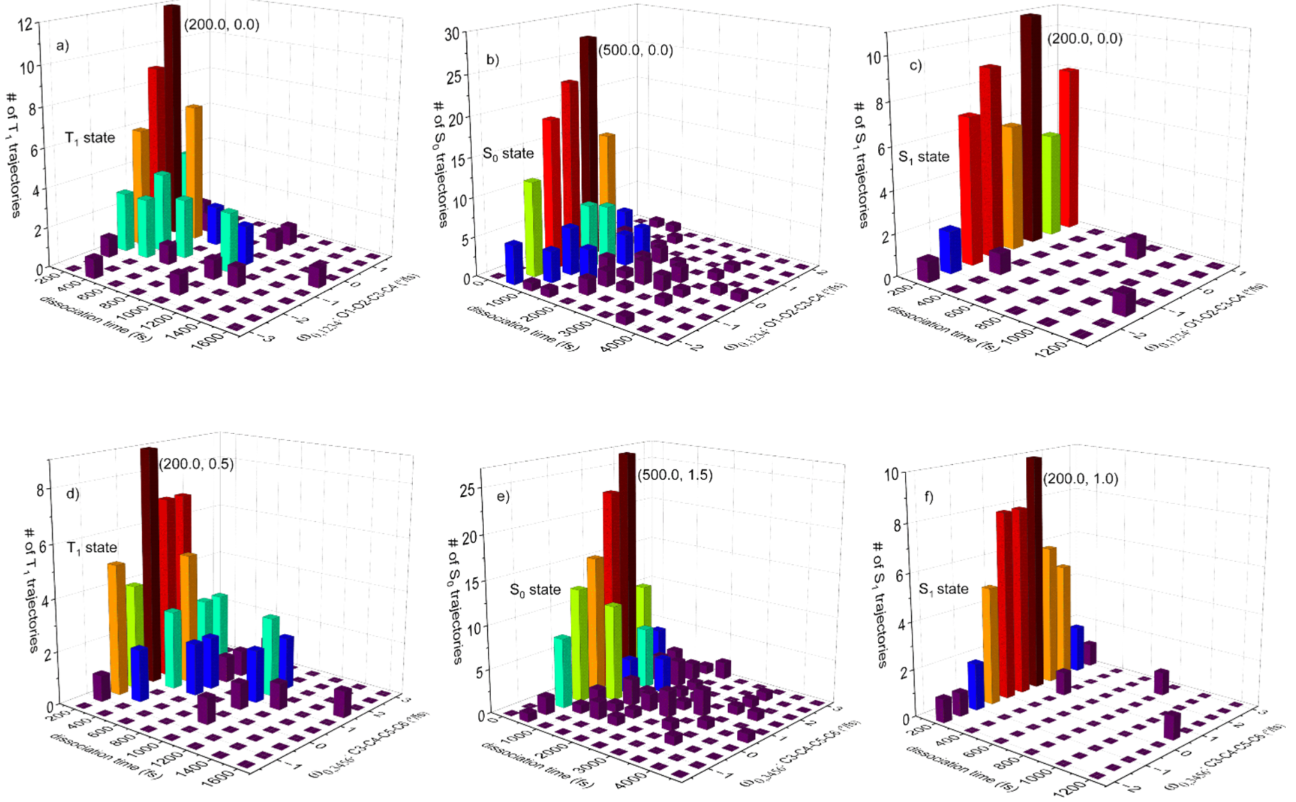

Figure 5. Distribution of the number of trajectories over the dissociation time (femtoseconds) and the initial angular velocity (degrees per femtosecond) of the O1−O2−C3−C4 dihedral angle for (a) state T_1, (b) state S_0, and (c) state S_1. Distribution over the dissociation time and the initial angular velocity of the C3−C4−C5−C6 dihedral angle for (d) state T_1, (e) state S_0, and (f) state S_1.

the initial velocities near the end points with considerable relative sizes of the subranges make the product molecule tend to certain energy states, and these special initial velocities can be identified as the most characteristic features for classifying the trajectories as per their final energy states. Because of the stochastic nature of the TSH method, it would be interesting to check if there are fuzzy boundaries,[57] which separate the trajectories by their product energy states, by applying a Bayesian support vector machine model.[58,59] We will discuss these issues in the future.

■ ASSOCIATED CONTENT

Supporting Information

The Supporting Information is available free of charge at https://pubs.acs.org/doi/10.1021/acs.jpclett.3c03578.

> Ground state, TS_{O-O}, and TS_{C-C} structures of the TDMD and their coordinates optimized by the SA-CASSCF; comparison of the potential energy gaps among SA-CASSCF/6-31G, SA-CASSCF/6-31G*, and CASPT2/ANO-RCC-VDZP; time evolutions of the C3−C4 distance, O1−O2−C3−C4 dihedral angle, and potential energy of the active state for the S_0 and S_1 trajectories; nonadiabatic transitions between the MCH states for the S_0 and S_1 trajectories and for the ensemble; spin−orbital coupling matrix elements over spin components of spin-free eigenstates; and distributions of the trajectories with product states T_1, S_0, and S_1 over the dissociation time and the initial velocity of O1−O2, C3−C4, and C5−C6, respectively (PDF)

■ AUTHOR INFORMATION

Corresponding Authors

Jian-Ge Zhou − *Interdisciplinary Nanotoxicity Center, Department of Chemistry, Physics and Atmospheric Sciences, Jackson State University, Jackson, Mississippi 39217, United States;* orcid.org/0000-0003-4817-4811; Email: jiange.zhou@jsums.edu

Jerzy Leszczynski − *Interdisciplinary Nanotoxicity Center, Department of Chemistry, Physics and Atmospheric Sciences, Jackson State University, Jackson, Mississippi 39217, United States;* orcid.org/0000-0001-5290-6136; Email: jerzy@icnanotox.org

Oleg Prezhdo − *Department of Chemistry and Department of Physics and Astronomy, University of Southern California, Los Angeles, California 90089, United States;* orcid.org/0000-0002-5140-7500; Email: prezhdo@usc.edu

Authors

Yinan Shu − *Department of Chemistry and Supercomputing Institute, University of Minnesota, Minneapolis, Minnesota 55455-0431, United States;* orcid.org/0000-0002-8371-0221

Yuchen Wang − *Department of Chemistry and James Franck Institute, The University of Chicago, Chicago, Illinois 60637, United States;* orcid.org/0000-0003-0479-3776

Complete contact information is available at: https://pubs.acs.org/10.1021/acs.jpclett.3c03578

Notes

The authors declare no competing financial interest.

■ ACKNOWLEDGMENTS

The authors thank Drs. S. Mai, M. Vacher, and W. J. Baader for helpful discussions. This work is supported by the National Science Foundation (NSF) under Grants CHE-2154367, HRD-2100971, EES-2300321, and HRD-1547754. The computation time was provided by the Mississippi Center for Supercomputing Research.

■ REFERENCES

(1) Vacher, M.; Fdez. Galvan, I.; Ding, B. W.; Schramm, S.; Berraud-Pache, R.; Naumov, P.; Ferre, N.; Liu, Y. J.; Navizet, I.; Roca-Sanjuan, D.; et al. Chemi- and Bioluminescence of Cyclic Peroxides. *Chem. Rev.* **2018**, *118* (15), 6927−6974.

(2) Yue, L.; Liu, Y. J. Conical Intersection in Chemiluminescence of Cyclic Peroxides. *J. Phys. Chem. Lett.* **2022**, *13* (46), 10671−10687.

(3) Phun, G. S.; Rappoport, D.; Furche, F.; Gibson, T. R.; Tretiak, S. Constructing the Mechanism of Dinoflagellate Luciferin Bioluminescence Using Computation. *J. Phys. Chem. Lett.* **2023**, *14* (26), 6001−6008.

(4) Adnane, F.; El-Zayat, E.; Fahmy, H. M. The combinational application of photodynamic therapy and nanotechnology in skin cancer treatment: A review. *Tissue Cell* **2022**, *77*, No. 101856.

(5) Jin, M.; Xiang, J.; Chen, C.; Zhang, Z.; Li, Y.; Tang, J.; Guo, C. Multifunctional Antibacterial Nanoplatform Bi_2WO_6:Nd^{3+}/Yb^{3+}/Er^{3+}@MoS_2 with Self-Monitoring Photothermal and Photodynamic Treatment. *J. Phys. Chem. Lett.* **2023**, *14* (36), 8213−8220.

(6) Kou, M.; Qin, F.; Lu, W.; Hu, Z.; Zhang, Z. A New Insight into the Singlet Oxygen Mechanism for Photodynamic Therapy. *J. Phys. Chem. Lett.* **2023**, *14* (24), 5613−5617.

(7) Kasatkina, L. A.; Ma, C.; Matlashov, M. E.; Vu, T.; Li, M.; Kaberniuk, A. A.; Yao, J.; Verkhusha, V. V. Optogenetic manipulation and photoacoustic imaging using a near-infrared transgenic mouse model. *Nat. Commun.* **2022**, *13* (1), 2813.

(8) Zhang, L.; Xu, F.; Chen, Z.; Zhu, X.; Min, W. Bioluminescence Assisted Switching and Fluorescence Imaging (BASFI). *J. Phys. Chem. Lett.* **2013**, *4*, 3897−3902.

(9) Zhang, J.; Li, W.; Zhu, W.; Qin, P.; Lu, M.; Zhang, X.; Miao, Y.; Cai, Z. Mesoporous graphitic carbon nitride@$NiCo_2O_4$ nanocomposite as a solid phase microextraction coating for sensitive determination of environmental pollutants in human serum samples. *Chem. Commun. (Camb)* **2019**, *55* (67), 10019−10022.

(10) Adam, W.; Baader, W. J. Effects of Methylation on the Thermal Stability and Chemiluminescence Properties of 1,2-Dioxetanes. *J. Am. Chem. Soc.* **1985**, *107* (2), 410−416.

(11) Augusto, F. A.; Frances-Monerris, A.; Fdez. Galvan, I.; Roca-Sanjuan, D.; Bastos, E. L.; Baader, W. J.; Lindh, R. Mechanism of activated chemiluminescence of cyclic peroxides: 1,2-dioxetanes and 1,2-dioxetanones. *Phys. Chem. Chem. Phys.* **2017**, *19* (5), 3955−3962.

(12) Farahani, P.; Baader, W. J. Unimolecular Decomposition Mechanism of 1,2-Dioxetanedione: Concerted or Biradical? That is the Question! *J. Phys. Chem. A* **2017**, *121* (6), 1189−1194.

(13) Zhou, J. G.; Yang, S.; Deng, Z. Y. Electrostatic Catalysis Induced by Luciferases in the Decomposition of the Firefly Dioxetanone and Its Analogue. *J. Phys. Chem. B* **2017**, *121* (49), 11053−11061.

(14) Magalhães, C. M.; Esteves da Silva, J. C. G.; Pinto da Silva, L. Theoretical Study of the Thermolysis Reaction and Chemiexcitation of Coelenterazine Dioxetanes. *J. Phys. Chem. A* **2022**, *126* (22), 3486−3494.

(15) Sahihi, M.; Sanz Garcia, J.; Navizet, I. Bioluminescent Nanoluciferase-Furimamide Complex: A Theoretical Study on Different Protonation States. *J. Phys. Chem. B* **2020**, *124* (13), 2539−2548.

(16) Zhou, J. G.; Williams, Q. L.; Walters, W., Jr.; Deng, Z. Y. How Does the Local Electrostatic Field Influence Emitted Wavelengths and Bioluminescent Intensities of Modified Heteroaromatic Luciferins? *J. Phys. Chem. B* **2015**, *119* (33), 10399−10405.

(17) Garcia-Iriepa, C.; Marazzi, M.; Navizet, I. The role of CO_2 detachment in fungal bioluminescence: thermally vs. excited state induced pathways. *Phys. Chem. Chem. Phys.* **2020**, *22* (46), 26787−26795.

(18) Zhou, J. G.; Yang, S.; Deng, Z. Y.; Leszczynski, J. Relative Order of Acidity among Hydroxyl Groups of Oxyluciferin and Emission Light Colors in Aqueous Solution. *J. Photochem. Photobiol., A* **2020**, *397*, 112504.

(19) Tully, J. C. Perspective: Nonadiabatic dynamics theory. *J. Chem. Phys.* **2012**, *137* (22), No. 22A301.

(20) Wang, L.; Prezhdo, O. V.; Beljonne, D. Mixed quantum-classical dynamics for charge transport in organics. *Phys. Chem. Chem. Phys.* **2015**, *17* (19), 12395−12406.

(21) Wang, L.; Akimov, A.; Prezhdo, O. V. Recent Progress in Surface Hopping: 2011−2015. *J. Phys. Chem. Lett.* **2016**, *7* (11), 2100−2112.

(22) Xie, C.; Zhao, B.; Malbon, C. L.; Yarkony, D. R.; Xie, D.; Guo, H. Insights into the Mechanism of Nonadiabatic Photodissociation from Product Vibrational Distributions. The Remarkable Case of Phenol. *J. Phys. Chem. Lett.* **2020**, *11* (1), 191−198.

(23) Wang, Y.; Guan, Y.; Guo, H.; Yarkony, D. R. Enabling complete multichannel nonadiabatic dynamics: A global representation of the two-channel coupled, $1,2^1A$ and 1^3A states of NH_3 using neural networks. *J. Chem. Phys.* **2021**, *154* (9), No. 094121.

(24) Zhang, L.; Shu, Y.; Sun, S.; Truhlar, D. G. Direct coherent switching with decay of mixing for intersystem crossing dynamics of thioformaldehyde: The effect of decoherence. *J. Chem. Phys.* **2021**, *154* (9), No. 094310.

(25) Mukherjee, S.; Varganov, S. A. Intersystem crossing and internal conversion dynamics with GAIMS-TeraChem: Excited state relaxation in 2-cyclopentenone. *J. Chem. Phys.* **2021**, *155* (17), No. 174107.

(26) Prezhdo, O. V. Modeling Non-adiabatic Dynamics in Nanoscale and Condensed Matter Systems. *Acc. Chem. Res.* **2021**, *54* (23), 4239−4249.

(27) Calio, P. B.; Truhlar, D. G.; Gagliardi, L. Nonadiabatic Molecular Dynamics by Multiconfiguration Pair-Density Functional Theory. *J. Chem. Theory Comput* **2022**, *18* (2), 614−622.

(28) Wang, Y.; Guo, H.; Yarkony, D. R. Internal conversion and intersystem crossing dynamics based on coupled potential energy surfaces with full geometry-dependent spin-orbit and derivative couplings. Nonadiabatic photodissociation dynamics of $NH_3(A)$ leading to the $NH(X^3Sigma^-$, $a^1Delta)$ + H_2 channel. *Phys. Chem. Chem. Phys.* **2022**, *24* (24), 15060−15067.

(29) Freixas, V. M.; Tretiak, S.; Fernandez-Alberti, S. Infinitene: Computational Insights from Nonadiabatic Excited State Dynamics. *J. Phys. Chem. Lett.* **2022**, *13* (36), 8495−8501.

(30) Dergachev, V. D.; Nakritskaia, D. D.; Alexeev, Y.; Gaita-Arino, A.; Varganov, S. A. Analytical nonadiabatic coupling and state-specific energy gradient for the crystal field Hamiltonian describing lanthanide single-ion magnets. *J. Chem. Phys.* **2023**, *159* (18), 184111.

(31) Shu, Y.; Zhang, L.; Wu, D.; Chen, X.; Sun, S.; Truhlar, D. G. New Gradient Correction Scheme for Electronically Nonadiabatic Dynamics Involving Multiple Spin States. *J. Chem. Theory Comput* **2023**, *19* (9), 2419−2429.

(32) Li, W.; Xue, T.; Mora-Perez, C.; Prezhdo, O. V. Ab Initio Quantum Dynamics of Plasmonic Charge Carriers. *Trends in Chemistry* **2023**, *5*, 634−645.

(33) Curchod, B. F. E.; Martinez, T. J. Ab Initio Nonadiabatic Quantum Molecular Dynamics. *Chem. Rev.* **2018**, *118* (7), 3305−3336.

(34) Wang, H. D.; Fu, Y. L.; Fu, B.; Fang, W.; Zhang, D. H. A highly accurate full-dimensional ab initio potential surface for the rearrangement of methylhydroxycarbene (H_3C-C-OH). *Phys. Chem. Chem. Phys.* **2023**, *25* (11), 8117−8127.

(35) Liu, T.; Fu, B.; Zhang, D. H. Mode specificity of water dissociating on Ni(100): An approximate full-dimensional quantum dynamics study. *J. Chem. Phys.* **2023**, *158* (21), 214305.

(36) Vacher, M.; Brakestad, A.; Karlsson, H. O.; Fdez. Galvan, I.; Lindh, R. Dynamical Insights into the Decomposition of 1,2-Dioxetane. *J. Chem. Theory Comput.* **2017**, *13* (6), 2448−2457.

(37) Vacher, M.; Farahani, P.; Valentini, A.; Frutos, L. M.; Karlsson, H. O.; Fdez. Galvan, I.; Lindh, R. How Do Methyl Groups Enhance the Triplet Chemiexcitation Yield of Dioxetane? *J. Phys. Chem. Lett.* **2017**, *8* (16), 3790−3794.

(38) Barbatti, M.; Granucci, G.; Ruckenbauer, M.; Plasser, F.; Pittner, J.; Persico, M.; Lischka, H. *NEWTON-X: A package for Newtonian dynamics close to the crossing seam;* 2013 (www.newtonx.org).

(39) Aquilante, F.; Autschbach, J.; Carlson, R. K.; Chibotaru, L. F.; Delcey, M. G.; De Vico, L.; Fdez. Galvan, I.; Ferre, N.; Frutos, L. M.; Gagliardi, L.; et al. Molcas 8: New capabilities for multiconfigurational quantum chemical calculations across the periodic table. *J. Comput. Chem.* **2016**, *37* (5), 506−541.

(40) Roos, B. O. The Complete Active Space Self-Consistent Field Method and its Applications in Electronic Structure Calculations. *Adv. Chem. Phys.* **1987**, *69*, 399−445.

(41) Roos, B. O.; Lindh, R.; Malmqvist, P. A.; Veryazov, V.; Widmark, P. O. Main Group Atoms and Dimers Studied with a New Relativistic ANO Basis Set. *J. Phys. Chem. A* **2004**, *108*, 2851−2858.

(42) Yue, L.; Yu, L.; Xu, C.; Zhu, C.; Liu, Y. Quantum yields of singlet and triplet chemiexcitation of dimethyl 1,2-dioxetane: ab initio nonadiabatic molecular dynamic simulations. *Phys. Chem. Chem. Phys.* **2020**, *22* (20), 11440−11451.

(43) Richter, M.; Marquetand, P.; Gonzalez-Vazquez, J.; Sola, I.; Gonzalez, L. SHARC: ab Initio Molecular Dynamics with Surface Hopping in the Adiabatic Representation Including Arbitrary Couplings. *J. Chem. Theory Comput* **2011**, *7* (5), 1253−1258.

(44) Mai, S.; Marquetand, P.; González, L. A General Method to Describe Intersystem Crossing Dynamics in Trajectory Surface Hopping. *Int. J. Quantum Chem.* **2015**, *115*, 1215−1231.

(45) Mai, S.; Marquetand, P.; Gonzalez, L. Nonadiabatic dynamics: The SHARC approach. *Wiley Interdiscip Rev. Comput. Mol. Sci.* **2018**, *8* (6), No. e1370.

(46) Li Manni, G.; Fdez. Galvan, I.; Alavi, A.; Aleotti, F.; Aquilante, F.; Autschbach, J.; Avagliano, D.; Baiardi, A.; Bao, J. J.; Battaglia, S.; et al. The OpenMolcas Web: A Community-Driven Approach to Advancing Computational Chemistry. *J. Chem. Theory Comput.* **2023**, *19* (20), 6933−6991.

(47) Grazioli, G.; Roy, S.; Butts, C. T. Predicting Reaction Products and Automating Reactive Trajectory Characterization in Molecular Simulations with Support Vector Machines. *J. Chem. Inf Model* **2019**, *59* (6), 2753−2764.

(48) Francl, M. M.; Pietro, W. J.; Hehre, W. J.; Binkley, J. S.; DeFrees, D. J.; Pople, J. A.; Gordon, M. S. Self-Consistent Molecular Orbital Methods. 23. A polarization-type basis set for 2nd-row elements. *J. Chem. Phys.* **1982**, *77*, 3654−3665.

(49) Granucci, G.; Persico, M.; Zoccante, A. Including quantum decoherence in surface hopping. *J. Chem. Phys.* **2010**, *133* (13), No. 134111.

(50) Plasser, F.; Mai, S.; Fumanal, M.; Gindensperger, E.; Daniel, C.; Gonzalez, L. Strong Influence of Decoherence Corrections and Momentum Rescaling in Surface Hopping Dynamics of Transition Metal Complexes. *J. Chem. Theory Comput* **2019**, *15* (9), 5031−5045.

(51) Shu, Y.; Truhlar, D. G. Decoherence and Its Role in Electronically Nonadiabatic Dynamics. *J. Chem. Theory Comput* **2023**, *19* (2), 380−395.

(52) Verlet, L. Computer "Experiments" on Classical Fluids. I. Thermodynamical Properties of Lennard−Jones Molecules. *Phys. Rev.* **1967**, *159*, 98−103.

(53) Shu, Y.; Zhang, L.; Varga, Z.; Parker, K. A.; Kanchanakungwankul, S.; Sun, S.; Truhlar, D. G. Conservation of Angular Momentum in Direct Nonadiabatic Dynamics. *J. Phys. Chem. Lett.* **2020**, *11* (3), 1135−1140.

(54) Marian, C. M. Spin−orbit coupling and intersystem crossing in molecules. *WIREs Comput. Mol. Sci.* **2012**, *2* (2), 187−203.

(55) Granucci, G.; Persico, M.; Spighi, G. Surface hopping trajectory simulations with spin-orbit and dynamical couplings. *J. Chem. Phys.* **2012**, *137* (22), No. 22A501.

(56) Sellner, B.; Barbatti, M.; Lischka, H. Dynamics starting at a conical intersection: application to the photochemistry of pyrrole. *J. Chem. Phys.* **2009**, *131* (2), No. 024312.

(57) Wang, Z. P.; Zhang, X.; Wu, H. N.; Huang, T. Fuzzy Boundary Control for Nonlinear Delayed DPSs Under Boundary Measurements. *IEEE Trans Cybern* **2023**, *53* (3), 1547−1556.

(58) Wenzel, F.; Galy-Fajou, T.; Deutsch, M.; Kloft, M. Bayesian nonlinear support vector machines for big data. *ECML PKDD, Lecture notes in computer science*; Springer, 2017; 10534.

(59) Sun, W.; Chang, C.; Zhao, Y.; Long, Q. Knowledge-Guided Bayesian Support Vector Machine for High-Dimensional Data with Application to Analysis of Genomics Data. *Proc. IEEE Int. Conf Big Data* **2018**, *2018*, 1484−1493.